Steel and Composite Structures, *Vol. 54, No. 5 (2025) 411-421*
https://doi.org/10.12989/scs.2025.54.5.411

Stiffness degradation of cracked metal/ceramic sandwich plates under hygro-thermo-mechanical loading

Mohamed Khodjet-Kesba*, Zineb Mouloudj and Billel Boukert

Aeronautical Sciences Laboratory, Institute of Aeronautics, and Space Studies, University of Blida 1, BP 270 Blida 09000, Algeria

(Received August 14, 2024, Revised October 28, 2024, Accepted November 21, 2024)

Abstract. The proposed model introduces a novel approach to predicting stiffness and Poisson's ratio degradation in metal-ceramic sandwich plates, specifically under hygro-thermo-mechanical loadings. Unlike previous models such as the Equivalent Constraint Model (ECM), this model incorporates an inter-laminar adhesive layer to transmit normal and shear stresses between the ceramic and metallic layers, significantly enhancing its accuracy in environmental stress simulation. By extending the shear-lag model to include temperature and humidity effects, this model provides a more precise prediction of mechanical response under extreme operational conditions. Validation against experimental data further establishes the model's reliability, showing a substantial improvement in predictive capability. The Analysis reveals that both stiffness and Poisson's ratio degrade progressively with increasing crack density, temperature, and concentration, with the extent of degradation varying across metal content. Validated against experimental data, this model advances scientific understanding of metal-ceramic composite performance and provides a practical, accurate tool for designing resilient composites in demanding sectors such as aerospace and automotive, where environmental resilience is critical.

Keywords: hygro-thermo-mechanical; metal ceramic; poisson's ratio; shear-lag; stiffness; transverse cracking

1. Introduction

Metal/ceramic composites are in high demand across various industries due to their superior thermo-mechanical properties. Among the different types of composites, interpenetrating phase composites (IPCs) with percolating metallic and ceramic phases offer a unique combination of strength, toughness, stiffness, excellent thermal properties, and wear resistance, along with the flexibility in microstructure and processing route selection (Kota *et al.* 2022). Ceramic preforms fabricated through freeze-casting are particularly suitable for IPC fabrication, thanks to their lamellar open porous structure and excellent permeability for melt infiltration (Roy *et al*. 2023).

Recent years have witnessed a growing interest in the freeze-casting process, which is a simple, economical, and environmentally friendly method for producing highly porous materials. Materials obtained via this technique typically exhibit a directional pore structure and anisotropic properties. However, the ability to control processing parameters such as solvent type, solids concentration, particle size, freezing rate, and types of additives allows for a wide range of pore sizes and morphologies. These varied morphologies expand the applicability of freeze-casted materials in numerous technological applications (Santos *et al.* 2021).

Despite significant advancements, a research gap exists in understanding the hygro-thermo-mechanical behavior of cracked metal/ceramic composites. While previous studies have examined various aspects of metal-ceramics, few have explored the interplay between environmental factors and structural integrity under multi- axial loading conditions.

In this context, Roy *et al.* (2020) investigated how the freezing temperature of ceramic preforms and the melt infiltration technique influence the mechanical properties of lamellar metal/ceramic composites. Their findings revealed that a lower freezing temperature refined lamellae, enhancing compressive strength and stiffness in the freezing direction, while die-casting deformed the lamellar structure, significantly reducing strength and stiffness compared to squeeze-casting.

Similarly, Schukraft *et al.* (2021) studied an interpenetrating metal-ceramic composite composed of ceramic foam and a lightweight AlSi10Mg aluminum alloy under compressive load, focusing on damage processes and crack development through 2D and 3D characterization methods. Their results indicated that cracks initiated in the ceramic phase, propagating parallel to the load and evolving into a shear-dominated failure mechanism, thereby contributing valuable insights into failure behaviors.

Theoretical models are essential for complementing experimental studies on the behavior of metal/ceramic sandwich materials, as they allow researchers to analyze complex mechanical responses under various loading conditions. Experimental studies, while valuable, face challenges in replicating real-world environmental factors such as temperature and humidity, which can significantly impact material stiffness and durability. Simulating these environmental effects experimentally can be resource-intensive and challenging, leading to a need for advanced theoretical models that can accurately predict material

*Corresponding author, Ph.D.
E-mail: mkhojet@gmail.com

ISSN: 1229-9367 (Print), 1598-6233 (Online)

behavior under such conditions. These models help bridge gaps in experimental data, especially regarding stiffness degradation under real operational environments, by providing insights into how these composites might perform in the field.

Kashtalyan *et al.* (2015) developed the Equivalent Constraint Model (ECM) to assess stiffness degradation in metal/ceramic composites primarily due to transverse cracking. However, this model has limitations when applied to environments with complex, variable conditions. ECM effectively captures stiffness reduction caused by cracking but does not consider critical factors like temperature and moisture variations, which play a significant role in practical applications. As a result, ECM's predictive accuracy is limited under real-world conditions where environmental influences substantially impact material behavior. Furthermore, ECM lacks detailed modeling of inter-laminar interactions, as it does not incorporate adhesive layers that could facilitate load transfer between layers. This omission reduces ECM's capability to simulate layered composite behavior under the combined influence of environmental stressors.

Khodjet-Kesba *et al.* (2021) advance beyond these limitations by developing a model that considers both temperature and humidity effects on stress distribution in cracked metal/ceramic composites. Their model includes an inter-laminar adhesive layer that transmits normal and shear stresses, allowing for a more precise simulation of the mechanical response under complex environmental conditions. This approach provides a significant advantage over ECM, as it better reflects the composite's actual behavior under varying operational conditions, verified through alignment with experimental data. Consequently, this model offered a more realistic and robust predictive tool for applications where environmental factors critically impacted material performance.

Building on previous work, this study develops a refined model that addresses stiffness and Poisson's ratio degradation in cracked metal/ceramic sandwich plates under hygro-thermo-mechanical conditions. By extending the shear lag model to include an interlaminar adhesive layer, this approach more accurately predicts material responses to environmental stressors like temperature and moisture. The model's predictions align closely with experimental data from Joffe *et al.* (2001), offering a marked improvement over the Equivalent Constraint Model (ECM) by integrating environmental factors critical to real-world applications. The effects of temperature and moisture concentration will be examined to predict the mechanical behavior of cracked metal/ceramic plates with varying metal ratio percentages. This enhanced model provides a practical tool for engineers and material scientists, enabling reliable performance predictions for metal/ceramic composites in demanding operational environments, such as aerospace, automotive, and energy sectors, where resistance to environmental degradation is essential for material longevity and safety. Additionally, this model offers valuable insights that can guide experimental research by identifying key environmental parameters and stressors for focus, helping to streamline laboratory efforts and refine testing conditions to more closely emulate real-world scenarios.

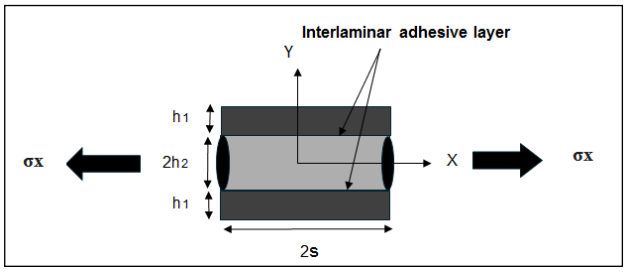

Fig. 1 Transversely cracked plate laminate and geometric model

2. Theoretical analysis

2.1 Stress functions for hybrid sandwich plate laminates

A laminated plate subjected to uniaxial loading is examined. It is assumed that a transverse crack has developed in the inner layer along the x-axis. The laminated plate is characterized by $2.h_2$, the width of the inner ply; h1, the width of the outer ply; and 2s, the spacing between two cracks (see Fig. 1).

$$\sigma_x{}^{(1)}h_1 + \sigma_x{}^{(2)}h_2 = \sigma_x h \tag{1}$$

The stress functions $F^{(i)}$(x,y) for each layer can be expressed as:

$$F^{(i)}(x,y) = f^{(i)}(x)g^{(i)}(y) \tag{2a}$$

$$g^{(1)}(y) = A^{(1)} \cdot (y-h)^2 + B^{(1)} \cdot (y-h) + C^{(1)} \tag{2b}$$

$$g^{(2)}(y) = A^{(2)} \cdot y^2 + B^{(2)} \cdot y + C^{(2)} \tag{2c}$$

Where $A^{(i)}$, $B^{(i)}$, $C^{(i)}$ are functions to be determined and i(=1,2) denote the outer and inner layer,

From Eq. (2), the following equations are derived using the stress expressions for each layer (El Meiche *et al.* 2009):

$$\sigma_x{}^{(i)} = \frac{\partial^2 F^{(i)}}{\partial y^2} \tag{3a}$$

$$\sigma_y{}^{(i)} = \frac{\sigma^2 F^{(i)}}{\partial x^2} \tag{3b}$$

$$\tau_{xy}{}^{(i)} = -\frac{\partial^2 F^{(i)}}{\partial x \partial y} \tag{3c}$$

In the absence of body forces, the above stress expressions automatically satisfy the equilibrium equations (El Meiche *et al*. 2009):

$$\frac{\partial \sigma_x{}^{(i)}}{\partial x} + \frac{\partial \tau_{xy}{}^{(i)}}{\partial y} = 0 \tag{4a}$$

$$\frac{\partial \tau_{xy}{}^{(i)}}{\partial x} + \frac{\partial \sigma_y{}^{(i)}}{\partial y} = 0 \tag{4b}$$

The traction continuity, boundary, and symmetry conditions, as illustrated in Fig. 1, require that:

$$\tau_{xy}{}^{(1)} = 0 \quad \text{at} \quad y = h \tag{5a}$$

$$\sigma_y{}^{(1)} = 0 \quad \text{at} \quad y = h \tag{5b}$$

$$\tau_{xy}{}^{(2)} = 0 \quad \text{at} \quad y = 0 \tag{5c}$$

$$\tau_{xy}{}^{(1)} = \tau_{xy}{}^{(2)} \quad \text{at} \quad y = h_2 \tag{5d}$$

$$\sigma_y{}^{(1)} = \sigma_y{}^{(2)} \quad \text{at} \quad y = h_2 \tag{5e}$$

$$u^{(1)} = u^{(2)} = 0 \quad \text{at} \quad x = 0 \tag{5f}$$

$$v^{(1)} = 0 \quad \text{at} \quad y = 0 \tag{5g}$$

$$\sigma_x{}^{(2)} = 0 \quad \text{at} \quad x = \pm s \tag{5h}$$

$$\tau_{xy}{}^{(1)} = \tau_{xy}{}^{(2)} = 0 \quad \text{at} \quad x = 0, \pm s \tag{5i}$$

By substituting the aforementioned conditions into the stress component expressions, the following equations can be derived:

$$A^{(1)} = 1, B^{(1)} = 0, C^{(1)} = 0\ , A^{(2)} = 1\ , B^{(2)} = 0,\ C^{(2)} = -h_2 h \tag{6a}$$

$$\left[f^{(1)}(x)\right]' = -\frac{h2}{h1}\left[f^{(2)}(x)\right]', \quad \left[f^{(1)}(\mathrm{x})\right]'' = -\frac{h_2}{h_1}\left[f^{(2)}(\mathrm{x})\right]'' \tag{6b}$$

When the self-equilibrium equation (Eq. (4)) is considered, Eq. (6) becomes:

$$f^{(1)}(x) = -\frac{h_2}{h_1} f^{(2)}(x) + \frac{h}{2h_2}\sigma_x \tag{7}$$

From the above equations, one undetermined function can be derived from the two stress functions.

$$f^{(2)}(x) = \phi(x) \tag{8}$$

The stress components for the outer layer are as follows:

$$\sigma_x{}^{(1)} = 2\left[-\frac{h_2}{h_1}\phi(x) + \frac{h}{2h_1}\sigma_x\right] \tag{9a}$$

$$\sigma_y{}^{(1)} = (y-h)^2\left[-\frac{h_2}{h_1}\phi''(x)\right] \tag{9b}$$

$$\tau_{xy}{}^{(1)} = -2(y-h)\left[-\frac{h_2}{h_1}\phi'(x)\right] \tag{9c}$$

The stress components in the inner layer are as follows (Khodjet-Kesba *et al.* 2021):

$$\sigma_x{}^{(2)} = 2\phi(x) \tag{10a}$$

$$\sigma_y{}^{(2)} = (y^2 - hh_2)\phi''(x) \tag{10b}$$

$$\tau_{xy}{}^{(2)} = -2y\phi'(x) \tag{10c}$$

The strains in the inner and outer layers are derived from:

$$\varepsilon_x{}^{(1)} = \frac{1}{E_x{}^{(1)}}\sigma_x{}^{(1)} - \frac{\upsilon_{xy}{}^{(1)}}{E_x{}^{(1)}}\sigma_y{}^{(1)} + \alpha_1\Delta T + \beta_1\Delta C \tag{11a}$$

$$\varepsilon_y{}^{(1)} = \frac{1}{E_y{}^{(1)}}\sigma_y{}^{(1)} - \frac{\upsilon_{xy}{}^{(1)}}{E_x{}^{(1)}}\sigma_x{}^{(1)} \tag{11b}$$

$$\varepsilon_x{}^{(2)} = \frac{1}{E_x{}^{(2)}}\sigma_x{}^{(2)} - \frac{\upsilon_{xy}{}^{(2)}}{E_x{}^{(2)}}\sigma_y{}^{(2)} + \alpha_2\Delta T + \beta_2\Delta C \tag{11c}$$

$$\varepsilon_y{}^{(2)} = \frac{1}{E_y{}^{(2)}}\sigma_y{}^{(2)} - \frac{\upsilon_{xy}{}^{(2)}}{E_x{}^{(2)}}\sigma_x{}^{(2)} \tag{11d}$$

From the strain–displacement relationships in Equation (11) and by applying the displacement boundary conditions in Eqs. (5f) and (5g), the displacement fields are obtained as follows:

$$u^{(1)} = \frac{2}{E_x{}^{(1)}}\left[-\frac{h_2}{h_1}\int\phi(x)dx + \frac{h}{2h_1}\sigma_x x\right] - \frac{\upsilon_{xy}{}^{(1)}}{E_x{}^{(1)}}\left[-\frac{h_2}{h_1}\int\phi''(x)dx\right]\cdot (y-h)^2 + (\alpha_1\Delta T + \beta_1\Delta C)x \tag{12a}$$

$$v^{(1)} = -\frac{2\upsilon_{xy}{}^{(1)}}{E_x{}^{(1)}}\left[-\frac{h_2}{h_1}\phi(x) + \frac{h}{2h_1}\sigma_x\right]y + \frac{1}{E_y{}^{(1)}}\cdot \left[-\frac{h_2}{h_1}\phi''(x)\right]\frac{(y-h)^3}{3} + f(x) \tag{12b}$$

$$u^{(2)} = \left[\frac{2}{E_x^{(2)}}\left[\int\phi(x)dx\right] - \frac{\upsilon_{xy}^{(2)}}{E_x^{(2)}}\right]\left[\int\phi''(x)dx\right](y-h_2h)^2 + (\alpha_2\Delta T + \beta_2\Delta C)x \tag{12c}$$

$$v^{(2)} = -\frac{2\upsilon_{xy}{}^{(2)}}{E_x{}^{(2)}}\phi(x)\cdot y + \frac{1}{E_x{}^{(2)}}\cdot \left[\phi''(x)\right]\left(\frac{1}{3}y^3 - h_2 h\cdot y\right) \tag{12d}$$

In Eq. (12b), $f(x)$ is a function which is determined by interface continuity conditions.

2.2 The extend shear lag model

As outlined by the model proposed by El Meiche *et al.* (2009), the presence of an inter-laminar isotropic resin layer with a thickness d is assumed, which separates the outer layer from the central layer (see Fig. 2). The effects of Poisson's ratio and transverse displacement are not considered; instead, the inter-laminar shear stress is calculated using the difference in average axial displacement.

The expressions for the average strains are derived from the angular deformation and displacement continuity

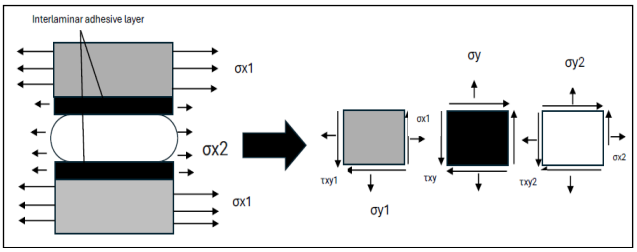

Fig. 2 Stress component in the corresponding layer.

between the two layers.

$$\overline{\varepsilon_y} = \frac{\partial \overline{v}}{\partial y} \approx \frac{v_1 - v_2}{d} \tag{13}$$

$$\overline{v_{xy}} = \frac{\overline{\partial u}}{\partial y} + \frac{\overline{\partial v}}{\partial x} \approx \frac{u_1 - u_2}{d} + \frac{1}{2}\left(\frac{\partial v_1}{\partial x} + \frac{\partial v_2}{\partial x}\right) \tag{14}$$

Where u_1 and v_1 represent the displacements at the interface between the outer layer and the adhesive layer, and u_2 and v_2 denote the displacements at the interface between the central layer and the adhesive layer.

The inter-laminar stresses are determined using the linear stress–strain relationships (Khodjet-Kesba *et al.* 2021):

$$\sigma_y = E\frac{v_1 - v_2}{d} \tag{15}$$

$$\tau_{xy} = G\left[\frac{u_1 - u_2}{d} + \frac{1}{2}\left(\frac{\partial v_1}{\partial x} + \frac{\partial v_2}{\partial x}\right)\right] \tag{16}$$

Where E and G represent the elastic moduli of the inter-laminar adhesive layer.

The function *f(x)* is determined by substituting Eqs. (12b) and (12d) into Eq. (15) with y=h_2. Subsequently, incorporating Eqs. (12) and (16) yields

$$\tau_{xy} = G\left[\frac{u_1 - u_2}{d} + \frac{\partial v_2}{\partial x} + \frac{d}{2E}\frac{\partial \sigma_y}{\partial x}\right] \tag{17}$$

By substituting Eqs. (12) and either (9b) or (10b) into Eq. (17) with y = h2, the following is obtained (Khodjet-Kesba *et al.* 2021):

$$A\phi'''(x) + B\phi'(x) + C\int\phi(x)dx = Dx \tag{18}$$

Where

$$A = G\left(\frac{\frac{1}{3}h_2^3 - hh_2^2}{E_y^{(2)}} + \frac{1}{2}\frac{d(h_2^2 - hh_2)}{E}\right) \tag{19}$$

$$= G\left(\frac{\frac{v_{xy}^{(2)}(h_2^2 - hh_2)}{E_x^{(2)}} + \frac{v_{xy}^{(1)}h_2(h_2 - h)^2}{E_x^{(1)}h_1}}{d} - \frac{2v_{xy}^{(2)}h_2}{E_x^{(2)}}\right) \tag{20}$$

$$+2\,h_2$$

$$C = -\frac{2G}{d}\left(\frac{1}{Ex^{(1)}}\frac{h_2}{h_1} + \frac{1}{E_x{}^{(2)}}\right) \tag{21}$$

$$D = \frac{-G}{d}\left(\left[\frac{1}{Ex^{(1)}}\frac{h}{h1}\sigma x\right] + (\alpha_1 - \alpha_2)\Delta T + (\beta_1 - \beta_2)\Delta C\right) \tag{22}$$

Differentiating Eq. (18) with respect to x, and defin ing $\xi = B/A$, $\eta = C/A$ and $\theta = D/A$the result become s:

$$\phi'''' + \xi\phi'' + \eta\phi = 0 \tag{23}$$

The solution to Eq. (23) is obtained by solving the following characteristic equation:

$$\lambda^4 + \xi\lambda^2 + \eta = 0 \tag{24}$$

Finally

$$\phi = \frac{\theta}{\eta} + C_1e^{-ax} + C_2e^{ax} + C_3e^{-bx} + C_4e^{bx} \tag{25}$$

With

$$C_1 = \frac{1}{2}\cdot\frac{b\cdot sin(b\cdot s)\cdot\theta}{\eta(\cosh(b\cdot s)\cdot a\cdot\sinh(a\cdot s) - b\cdot\sinh(b\cdot s)\cdot\cosh(a\cdot s))} \tag{26}$$

$$C_2 = \frac{1}{2}\cdot\frac{b\cdot sin(b\cdot s)\cdot\theta}{\eta(\cosh(b\cdot s)\cdot a\cdot\sinh(a\cdot s) - b\cdot\sinh(b\cdot s)\cdot\cosh(a\cdot s))} \tag{27}$$

$$C_3 = -\frac{1}{2}\cdot\frac{a\cdot sin(a\cdot s)\cdot\theta}{\eta(\cosh(b\cdot s)\cdot a\cdot\sinh(a\cdot s) - b\cdot\sinh(b\cdot s)\cdot\cosh(a\cdot s))} \tag{28}$$

$$C_4 = -\frac{1}{2}\cdot\frac{asin(a\cdot s)\cdot\theta}{\eta(\cosh(b\cdot s)\cdot a\cdot\sinh(a\cdot s) - b\cdot\sinh(b\cdot s)\cdot\cosh(a\cdot s))} \tag{29}$$

$$a = \frac{1}{2}\cdot\sqrt{-2\cdot\xi - 2\cdot\sqrt{\xi^2 - 4\eta}} \tag{30}$$

$$b = \frac{1}{2}\cdot\sqrt{-2\cdot\xi + 2\cdot\sqrt{\xi^2 - 4\eta}} \tag{31}$$

Finally, the stress functions that satisfy the boundary conditions, equilibrium equations, and traction continuity at the interfaces can be determined. In this model, it is assumed that the inter-laminar adhesive layer has a thickness equal to twice the fiber diameter (with the fiber diameter assumed to be 7.6 μm). Consequently, the values of (v1 - v2) in Eq. (15) and (u1-u2) in Eq. (16) are approximately zero.

2.3 Stiffness degradation in the plate laminate

Transverse cracking is a prevalent mode of damage in plate laminates subjected to uniaxial tension. These cracks form in the y-direction and extend across the width of the central ply from the free edges. Using the results from the preceding section, the reduction in stiffness of plate laminates can be evaluated. It is assumed that the crack spacing is 2s, and the average surface axial strain, ε_x,

between two cracks is given by:

$$\varepsilon_x = \frac{\int_0^s \varepsilon_x^{(1)} dx}{s} \quad \text{at} \quad y=h \tag{32}$$

Finally, the stiffness degradation is determined from the strain-deformation relationship:

$$\frac{E_x}{E_0} = \frac{\sigma_x}{\varepsilon_x E_0} \tag{33}$$

2.4 Poisson's Ratio degradation in the plate laminate

The stresses in an undamaged laminate, along with its stiffness matrix, can be determined using classical laminate theory. The stress-strain relationships for the constituent materials are as follows (Khodjet-Kesba *et al.* 2021):

For the metal layer:

$$\varepsilon_x = \frac{1}{E_1}\sigma_{x1} - \frac{\upsilon_{12}}{E_1}\sigma_{y1} - \frac{\upsilon_{12}}{E_1}\sigma_{z1} \tag{34}$$

$$\varepsilon_y = -\frac{\upsilon_{12}}{E_2}\sigma_{x1} + \frac{1}{E_2}\sigma_{y1} - \frac{\upsilon_{23}}{E_2}\sigma_{z1} \tag{35}$$

For the ceramic layer:

$$\varepsilon_{x2} = \frac{1}{E_2}\sigma_{x2} - \frac{\upsilon_{12}}{E_1}\sigma_{y2} - \frac{\upsilon_{23}}{E_2}\sigma_{z2} \tag{36}$$

$$\varepsilon_y = -\frac{\upsilon_{12}}{E_2}\sigma_{x2} + \frac{1}{E_1}\sigma_{y2} - \frac{\upsilon_{12}}{E_1}\sigma_{z2} \tag{37}$$

It is assumed that a generalized state of plane strain is achieved such that the average strain along the y-axis is the same in both layers, and that ε_y remains constant.

$$\varepsilon_y = \overline{\varepsilon_{y1}} = \overline{\varepsilon_{y2}} \tag{38}$$

To obtain the Poisson's ratio for a damaged laminate, the following parameters must be calculated:

$$\upsilon_{xy} = -\frac{\varepsilon_y}{\overline{\varepsilon_{x1}}} \tag{39}$$

This equation includes the average value of the crack opening displacement normalized by the far-field strain ε_{x1}. Therefore, the average transverse crack opening displacement, denoted as U_a, is required.

$$u_a = s(\overline{\varepsilon_{x1}} - \overline{\varepsilon_{x2}}) \tag{40}$$

To utilize definitions (37) and (38), the average strains involved are expressed in terms of the applied load $\sigma x1$. Since the problem is treated as linear, all strains are proportional to the load. Consequently, Eq. (39) includes only the elastic and geometric properties of the constituents, the crack density, and the normalized crack opening within the laminate. The crack opening will be derived from the stress distributions surrounding the crack. After formulating the equilibrium equations for forces in the y and z directions, the following results are obtained:

$$\varepsilon_y = -\frac{\upsilon_{12}}{E_1(E_1h_2 + E_2h_1)}(E_1h_2\overline{\sigma_{x2}} + E_2h_1\overline{\sigma_{x1}}) \tag{41}$$

Table 1 Material properties of glass/epoxy laminate used in calculations (Joffe *et al*. 2001)

Proprieties / Material	E_L GPa	E_T GPa	G_{LT} GPa	$G_{TT'}$ GPa	υ_{LT}	$\upsilon_{TT'}$	h_0 mm	α_1	α_2
Glass/epoxy	44.73	12.76	5.8	4.49	0.297	0.42	0.144	8.6×10^{-6}	22.1×10^{-6}

Thus, this strain component is dependent on the average stress along the x-axis in both layers. By averaging the constitutive relationships (34) to (37), the following is obtained:

For the metal layer:

$$\overline{\varepsilon_{x1}} = \frac{1}{E_1}\overline{\sigma_{x1}} - \frac{\upsilon_{12}}{E_1}\overline{\sigma_{y1}} \tag{42}$$

$$\varepsilon_y = -\frac{\upsilon_{12}}{E_1}\overline{\sigma_{x1}} + \frac{1}{E_2}\overline{\sigma_{y1}} \tag{43}$$

For the ceramic layer:

$$\overline{\varepsilon_{x2}} = \frac{1}{E_2}\overline{\sigma_{x2}} - \frac{\upsilon_{12}}{E_1}\overline{\sigma_{y2}} \tag{44}$$

$$\varepsilon_y = -\frac{\upsilon_{12}}{E_1}\overline{\sigma_{x2}} + \frac{1}{E_1}\overline{\sigma_{y2}} \tag{45}$$

U_a is proportional to the applied far-field strain and the size of the crack. To utilize this quantity in stiffness predictions, it must first be normalized with respect to the far-field strain and half the thickness of the ceramic layer,

$$\overline{U_a} = \left(1 + \frac{1}{\alpha}\right)\left(\frac{E_{x0}}{E_1}\right)(1 - 12\upsilon_{xy0}) \cdot \left(\frac{2h_2L}{EP}\right) tanh\left(\frac{EP}{2h_2L}\right) \tag{46}$$

Hence

$$EP = \sqrt{GB \cdot \frac{h_2}{E_2}\left(1 + \frac{E_2}{\alpha E_1}\right)} \tag{47}$$

$$GB = \frac{3G}{h_2} \tag{48}$$

$$GB = \frac{G_2}{1 + \alpha\frac{G_2}{G_1}} \tag{49}$$

Where, G_1 and G_2 shear modulus for outer and inner layers respectively

3. Results and discussion

A computer code based on the present model was developed to predict the stiffness degradation of the cracked sandwich plate under hygro-thermo-mechanical loading.

3.1 Validation of the present model

The validation of the current model has been conducted

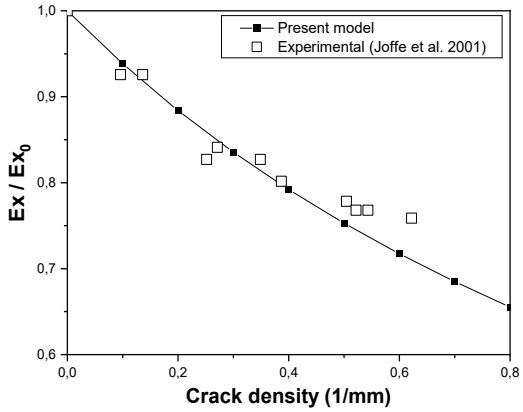

Fig. 3 Normalized stiffness properties of $[0_2/90_4]_s$ glass/epoxy laminate as a function of crack density

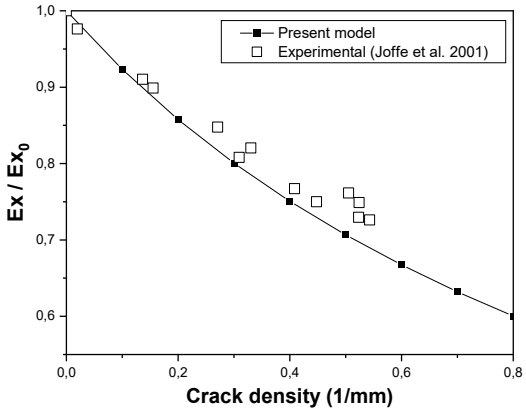

Fig. 4 Normalized stiffness properties of [±15/904]s glass/epoxy laminate as a function of crack density.

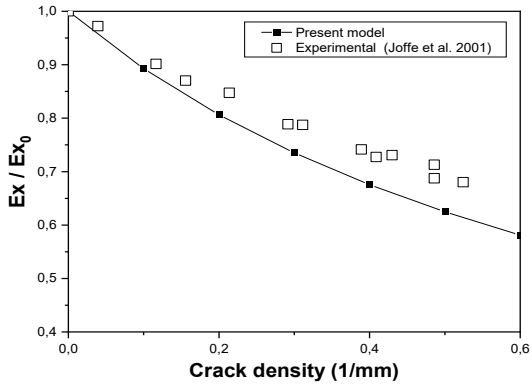

Fig. 5 Normalized stiffness properties of $[\pm 30/90_4]_s$ glass/epoxy laminate as a function of crack density

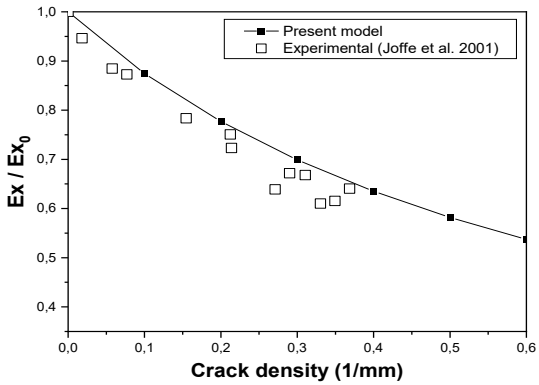

Fig. 6 Normalized stiffness properties of $[\pm 40/90_4]_s$ glass/epoxy laminate as a function of crack density

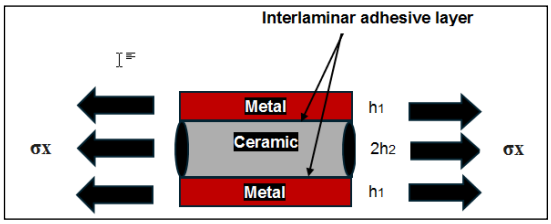

Fig. 7 A Geometric model for a Metal/Ceramic sandwich plate with transverse cracks

Table 2 Properties of the constituents (Kashtalyan *et al.* 2015)

Constituent	Young's modulus (GPa)	Poisson's ratio	Layer thickness (mm)	Shear modulus (GPa)
Aluminium alloy Al–12Si	80	0.33	0.3	30
Alumina Al_2O_3	390	0.24	0.2	157.26

in two scenarios. First, a comparison with experimental data was performed for a symmetric $[\theta/90]_s$ glass/epoxy laminate (Joffe *et al.* 2001) subjected to uniaxial loading. In this case, the angle-ply laminate is characterized by $2.t_{90}$, representing the thickness of the 90° ply, t_θ for the thickness of the θ° ply, and 2.s denoting the spacing between two cracks. The material properties of the glass/epoxy laminate (Joffe *et al.* 2001) are presented in Table 1.

Figs. 3 to 6 show the stiffness degradation in glass/epoxy composite laminates with various fiber orientation angles, focusing on the impact of transverse cracks. These figures compare the axial modulus reduction predicted by the current model with experimental data from Joffe *et al.* (2001). The findings suggest that stiffness loss is primarily due to increased crack density and higher fiber orientation angles in the outer layers. A strong alignment between the model's predictions and experimental results demonstrates the model's precision in reflecting the mechanical response to transverse cracking. This accuracy confirms the model's effectiveness for predicting material behavior in composite structures, supporting its use as a reliable tool for structural analysis under complex loading conditions.

Table 3 Comparison of stiffness degradation with Equivalent Constraint Model as a function of crack density with different ceramic ratio percentage

Pc %	Crack density (1/mm)	Present model	ECM (Kashtalyan *et al*. 2015).	|Error (%)|
35%	0.1	0.80559	0.79851	0.7080 %
	0.2	0.67446	0.6664	0.8060 %
	0.3	0.58005	0.57155	0.8500 %
	0.4	0.50884	0.50379	0.5050 %
	0.5	0.45333	0.44959	0.3740 %
	0.6	0.40911	0.40556	0.3550 %
	0.7	0.37345	0.37507	0.1620 %
	0.8	0.34449	0.34797	0.3480 %
	0.9	0.32088	0.33442	1.3540 %
45%	0.1	0.79093	0.76735	2.3580 %
	0.2	0.65416	0.63265	2.1510 %
	0.3	0.55786	0.5551	0.2760 %
	0.4	0.48724	0.4898	0.2560 %
	0.5	0.43487	0.44898	1.4110 %
	0.6	0.3961	0.41633	2.0230 %
	0.7	0.36745	0.39184	2.4390 %
	0.8	0.34625	0.37959	3.3340 %
	0.9	0.33047	0.36327	3.2800 %

3.2 Comparison between the present model and ECM

Consider a sandwich plate composed of two layers: the first layer is made of AL-12SI aluminum alloy, and the second layer is made of Al_2O_3 (alumina) (see Fig. 7). The properties of these materials are listed in the following table, with thermal coefficients $\alpha_1=23 \times (10^{-6}/°C)$, $\alpha_2=7.4 \times (10^{-6}/°C)$, respectively. For both materials, Poisson's ratio is assumed to be constant at $\nu=0.3$ (see Table 2).

To highlight the reduction in stiffness caused by transverse cracking, the variation in the longitudinal Young's modulus will be examined as a function of transverse crack density, under an applied axial load of σ_x = 470 MPa.

Table 3 illustrates the stiffness degradation as a function of crack density in a metal-ceramic composite with different ceramic contents. It is observed that the results are very similar across nearly all crack densities, particularly when ceramic ratio percentage Pc=35%. A reduction in stiffness of up to 68% is noted for a maximum crack density of 0.9 (1/mm), indicating that the material's rigidity is significantly affected by transverse cracks. Therefore, the comparison of our results with those reported by Kashtalayn *et al.* (2015) demonstrates a strong agreement, thereby validating our model.

3.3 hygro-thermo-mechanical effect on stiffness degradation

3.3.1 Influence of temperature and humidity on stiffness degradation

Table 3 presents data related to stiffness degradation under different conditions, specifically analyzing the effect of crack density and environmental factors on the stiffness of a material. The material is evaluated at different percentages of metal content (Pm) and under four distinct environmental conditions (denoted as i=1 to i=4). The conditions vary in temperature (ΔT) and concentration of humidity (ΔC), with increasing severity from i=1 (ΔT=0°C and ΔC=0%) to i=4 (ΔT=1200°C and ΔC=0.015%).

The obtained results (Table 4) demonstrate that an increase in crack density leads to a decrease in the stiffness ratio (E_x/E_{x0}), signifying a degradation in material stiffness. This degradation is more pronounced when the material does not show any cracks (maximum of 18% when crack density is equal to zero) and with lower metal ratio percentage (Pm). Therefore, this behavior reflects the inherent brittleness and sensitivity of the material to microstructural imperfections, which become critical in the absence of a ductile metal phase that could otherwise help to mitigate these effects.

The "Degradation gap" illustrates the disparity in stiffness degradation between the least and most severe environmental conditions, with this gap widening significantly as metal ratio percentage increases under high crack density. This suggests that the material's stiffness becomes increasingly sensitive to environmental conditions at higher metal ratio percentage and with high crack density. Consequently, this reflects the limitations of the metal phase in counteracting the effects of extensive cracking under extreme conditions.

3.3.2 Influence of Thickness Ratio on the stiffness degradation

The stiffness degradation of the metal/ceramic sandwich composite as a function of crack density and metal ratio

Table 4 Stiffness degradation as a function of crack density and environmental conditions across different metal content percentages

Pm %	Crack density (1/mm)	E_x / E_{x0} (Stiffness degradation)				Degradation gap E_x/E_{x0} (i=1) – E_x/E_{x0} (i=4)
		(i=1) ΔT=0°C and ΔC=0 %	(i=2) ΔT=300°C and ΔC=0.5 %	(i=3) ΔT=600°C and ΔC=1 %	(i=4) ΔT=1200°C and ΔC=1.5 %	
10%	0	1.00000	0.94580	0.89716	0.81356	18,6443%
	0.1	0.35870	0.35176	0.34509	0.33248	2,6217%
	0.2	0.21854	0.21606	0.21363	0.20893	0,9611%
	0.3	0.15714	0.15591	0.15470	0.15233	0,4815%
	0.4	0.12268	0.12196	0.12125	0.11986	0,2820%
	0.5	0.10061	0.10015	0.09969	0.09880	0,1814%
	0.6	0.08527	0.08496	0.08465	0.08403	0,1241%
	0.7	0.07400	0.07377	0.07355	0.07311	0,0886%
	0.8	0.06537	0.06520	0.06504	0.06472	0,0654%
	0.9	0.05857	0.05844	0.05832	0.05807	0,0494%
30%	0	1.00000	0.95733	0.91815	0.84872	15,1279%
	0.1	0.61240	0.59701	0.58237	0.55517	5,7228%
	0.2	0.44134	0.43375	0.42643	0.41250	2,8838%
	0.3	0.34497	0.34061	0.33636	0.32816	1,6810%
	0.4	0.28315	0.28040	0.27770	0.27246	1,0691%
	0.5	0.24014	0.23830	0.23649	0.23295	0,7197%
	0.6	0.20857	0.20728	0.20601	0.20352	0,5042%
	0.7	0.18452	0.18360	0.18269	0.18089	0,3638%
	0.8	0.16577	0.16509	0.16442	0.16309	0,2687%
	0.9	0.15092	0.15040	0.14990	0.14889	0,2024%
50%	0	1.00000	0.96914	0.94013	0.88706	11,2938%
	0.1	0.76190	0.74499	0.72881	0.69849	6,3412%
	0.2	0.61538	0.60505	0.59505	0.57604	3,9345%
	0.3	0.51613	0.50937	0.50278	0.49011	2,6013%
	0.4	0.44446	0.43983	0.43530	0.42652	1,7947%
	0.5	0.39041	0.38714	0.38392	0.37765	1,2759%
	0.6	0.34847	0.34611	0.34377	0.33920	0,9277%
	0.7	0.31539	0.31364	0.31192	0.30852	0,6872%
	0.8	0.28905	0.28774	0.28644	0.28387	0,5176%
	0.9	0.26795	0.26695	0.26596	0.26399	0,3959%

(Pm) are show in Figs. 8 and 9. When the hygro-thermo-mechanical load is minimized (ΔT=0°C and ΔC=0%), the stiffness degradation remains low across different metal ratios, suggesting that the material retains structural integrity in the absence of temperature and concentration variations. However, in Fig. 9, with higher hygro-thermal loading (ΔT=1200°C and ΔC=1.5%), stiffness degradation accelerates significantly as crack density increases. The higher metal ratio seems to mitigate this degradation to some extent, as metal layers offer better ductility and thermal expansion accommodation, thereby slowing the propagation of cracks within the Al_2O_3 ceramic core. This protective effect of metal layers under extreme hygro-thermal stress reveals the metal's role in improving resilience by balancing rigidity with flexibility, thus delaying the material's structural degradation as crack density increases.

3.4 hygro-thermo-mechanical effect on Poisson's ratio degradation

3.4.1 Influence of temperature and humidity on Poisson's ratio degradation

The degradation of Poisson's ratio is examined under various conditions, with a specific focus on the influence of crack density and environmental factors on the Poisson's ratio of a given material (see Table 5). The assessment is conducted at different percentages of metal content (Pm) and across four distinct environmental conditions (designated as i=1 to i=4). These conditions vary in terms of temperature (ΔT) and humidity concentration (ΔC), with increasing severity ranging from i=1 (ΔT=0°C and ΔC=0%)

Table 5 Poisson's ratio degradation as a function of crack density and environmental conditions across different metal content percentages

Pm %	Crack density (1/mm)	ν_{xy} / ν_{xy0} (Poisson's ratio degradation)				Degradation gap ν_{xy}/ν_{xy0} (i=1) – ν_{xy}/ν_{xy0} (i=4)
		(i=1) ΔT=0°C and ΔC=0 %	(i=2) ΔT=300°C and ΔC=0.5 %	(i=3) ΔT=600°C and ΔC=1 %	(i=4) ΔT=1200°C and ΔC=1.5 %	
10%	0	1.00000	0.99446	0.98948	0.98093	1.9069%
	0.1	0.93441	0.93370	0.93302	0.93173	0.2681%
	0.2	0.92007	0.91982	0.91957	0.91909	0.0983%
	0.3	0.91379	0.91367	0.91354	0.91330	0.0492%
	0.4	0.91027	0.91019	0.91012	0.90998	0.0288%
	0.5	0.90801	0.90796	0.90792	0.90783	0.0186%
	0.6	0.90644	0.90641	0.90638	0.90632	0.0127%
	0.7	0.90529	0.90527	0.90524	0.90520	0.0091%
	0.8	0.90441	0.90439	0.90437	0.90434	0.0067%
	0.9	0.90371	0.90370	0.90369	0.90366	0.0051%
30%	0	1.00000	0.98607	0.97329	0.95063	4.9373%
	0.1	0.87350	0.86847	0.86370	0.85482	1.8678%
	0.2	0.81767	0.81519	0.81280	0.80825	0.9412%
	0.3	0.78622	0.78479	0.78340	0.78073	0.5486%
	0.4	0.76604	0.76514	0.76426	0.76255	0.3489%
	0.5	0.75200	0.75140	0.75081	0.74965	0.2349%
	0.6	0.74170	0.74128	0.74086	0.74005	0.1646%
	0.7	0.73385	0.73355	0.73325	0.73266	0.1187%
	0.8	0.72773	0.72751	0.72729	0.72685	0.0877%
	0.9	0.72288	0.72271	0.72255	0.72222	0.0661%
50%	0	1.00000	0.98141	0.96393	0.93195	6.8052%
	0.1	0.85653	0.84634	0.83659	0.81832	3.8210%
	0.2	0.76824	0.76201	0.75599	0.74453	2.3708%
	0.3	0.70843	0.70436	0.70039	0.69276	1.5674%
	0.4	0.66525	0.66246	0.65973	0.65444	1.0814%
	0.5	0.63268	0.63071	0.62877	0.62499	0.7688%
	0.6	0.60741	0.60599	0.60458	0.60182	0.5590%
	0.7	0.58748	0.58643	0.58539	0.58334	0.4141%
	0.8	0.57161	0.57082	0.57003	0.56849	0.3119%
	0.9	0.55889	0.55829	0.55769	0.55651	0.2386%

to i=4 (ΔT=1200°C and ΔC=0.015%).

The data reveal that Poisson's ratio (ν_{xy}/ ν_{xy0}) degrades with increasing crack density and under intensified environmental conditions, specifically elevated temperature and humidity. As crack density rises, degradation in Poisson's ratio becomes more marked across all metal content levels (10%, 30%, and 50%). Both temperature and humidity appear to have a cumulative effect, the gap in degradation between minimal and extreme conditions widens as metal content increases, with a 10% metal content showing a minor degradation gap (around 1.9%) and 50% metal content showing a gap of approximately 6.8%. These findings indicate that materials with higher metal content are more susceptible to degradation in Poisson's ratio under extreme environmental conditions, especially as crack density increases, suggesting a stronger impact on the material's mechanical properties in such settings.

3.4.2 Influence of Thickness Ratio on Poisson's ratio degradation

The Poisson's ratio degradation in a metal/ceramic sandwich composite shows a strong dependence on crack density and metal ratio (Pm) (see Figs. 10 and 11). Under hygro-thermo-mechanical loadings, the increased density of transverse cracks disrupts the stress transfer, weakening the material's ability to maintain lateral contraction under axial load, which results in a reduction of the Poisson's ratio. When Pm exceeds 70%, the material's behavior significantly shifts; the increased metallic content enhances ductility and energy dissipation, making the composite more resilient to crack propagation and minimizing

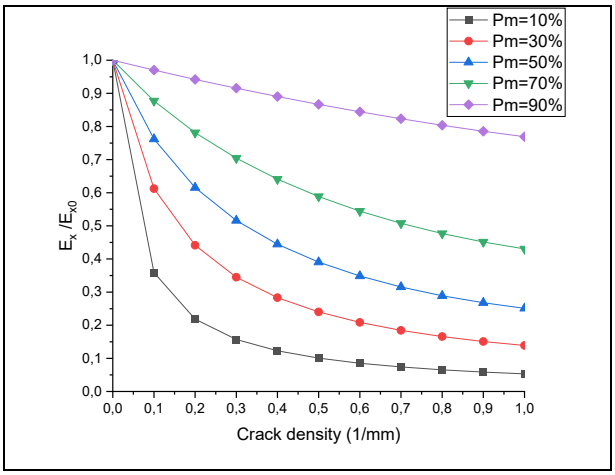

Fig. 8 Stiffness degradation of metal/ceramic sandwich as a function of crack density and with different metal ratio percentage (under i=1, ΔT=0°C and ΔC=0 %)

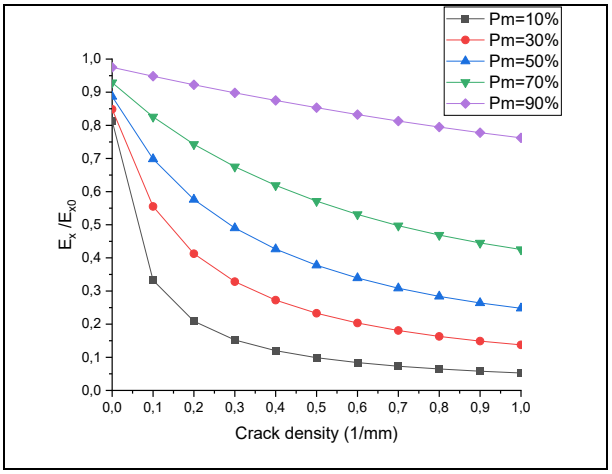

Fig. 9 Stiffness degradation of metal/ceramic sandwich as a function of crack density and with different metal ratio percentage (under i=4, ΔT=1200°C and ΔC=1.5 %)

Poisson's ratio degradation. This change reflects the role of the metal layers in redistributing stress and constraining ceramic brittleness, stabilizing the mechanical response under extreme thermal and concentration variations.

4. Conclusions

The aim of this study is to assess the degradation of stiffness and Poisson's ratio in cracked metal-ceramic sandwich plates under hygro-thermo-mechanical loading. Using an advanced shear-lag model, the research provides a detailed evaluation of how these materials degrade, particularly under the combined effects of temperature, moisture, and mechanical stress. This model offers a more accurate and comprehensive analysis of material performance in demanding conditions. The key findings of this study are as follows:

• Model validation and accuracy: The proposed shear-lag model, which includes an interlaminar adhesive layer

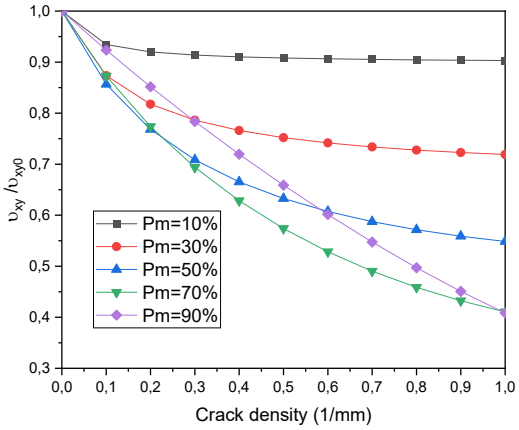

Fig. 10 Stiffness degradation of metal/ceramic sandwich as a function of crack density and with different metal ratio percentage (under i=1, ΔT=0°C and ΔC=0 %)

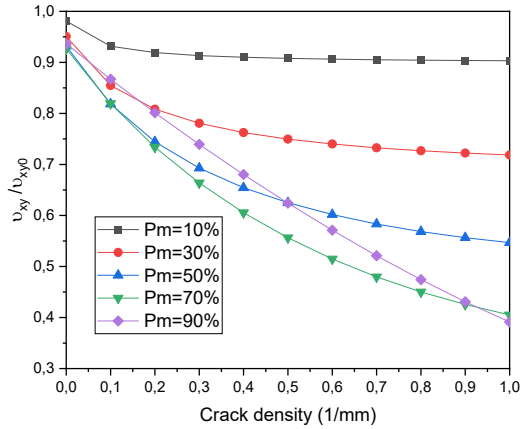

Fig. 11 Stiffness degradation of metal/ceramic sandwich as a function of crack density and with different metal ratio percentage (under i=4, ΔT=1200°C and ΔC=1.5 %)

and environmental factors such as temperature and moisture, was validated against experimental data and compared with the Equivalent Constraint Model. demonstrating its reliability and offering more accurate results than the ECM.

• Impact of material composition: The analysis reveals that ceramic content plays a crucial role in determining the overall stiffness of the sandwich plates. Although a higher ceramic ratio improves both properties, it also increases the material's vulnerability to degradation as crack density rises.

• Hygro-thermal effects: The study highlights the critical role of hygro-thermal conditions in the degradation process. Elevated temperature and moisture levels accelerate the stiffness and Poisson's ratio loss, particularly in materials with a higher ceramic content, indicating that environmental

conditions are crucial in the long-term performance of these composites.

• Crack density contribution: Crack density emerged as a major factor in stiffness and Poisson's ratio reduction. As the number of cracks increases, the stiffness and Poisson's ratio of the sandwich plates decreases significantly, especially under adverse hygro-thermal conditions.

• Practical implications: The results of this study provide critical guidance for designing metal/ceramic sandwich structures that are frequently subjected to extreme environmental conditions, such as those found in aerospace and automotive industries

The proposed model offers enhanced accuracy by incorporating environmental factors like temperature and humidity, alongside an inter-laminar adhesive layer that improves stress transmission, making it more reliable for predicting material behavior in real-world applications. Its simplicity and precision make it a practical tool for engineers in industries such as aerospace and automotive, where environmental resilience is crucial. Future research could focus on refining the model to account for more complex crack patterns and cyclic loading, while integrating it into predictive maintenance frameworks for real-time material degradation monitoring in critical structures.

References

El Meiche, N., Tounsi, A., Adda-Bedia E.A. and Megueni A. (2009), "Analysis of the transverse cracking in hybrid cross-ply composite laminates", *Comp. Mat. Sci*. **46**, 1102-1108. https://doi.org/10.1016/j.commatsci.2009.05.019.

Joffe, R., Krasnikovs A. and Varna, J. (2001), "COD-based simulation of transverse cracking and stiffness reduction in [S/90n]$_S$ laminates", *Compo. Sci. Tech*. **61**, 637–656. https://doi.org/10.1016/S0266-3538(00)00172-X.

Kashtalyan, M., Sinchuk, Y., Piat, R. and Guz I. (2015), "Analysis of multiple cracking in metal/ceramic composites with lamellar microstructure", *Arch Appl Mech*, **86**, 177-188. https://doi.org/10.1007/s00419-015-1103-7.

Khodjet Kesba, M., EL Meiche N. and Benkhedda, A. (2021), "Stress distribution on the cracked sandwich plate with non linear thermal and moisture concentration", *Nano Hybrids Compos.*, **32**, 45-62. https://doi.org/10.4028/www.scientific.net/NHC.32.45.

Kota, N., Sai Charan, M., Laha, T. and Roy, S. (2022), "Review on development of metal/ceramic interpenetrating phase composites and critical analysis of their properties", *Ceramics Int.*, **48**(2), 1451-1483. https://doi.org/10.1016/j.ceramint.2021.09.232

Laws, N. and Dvorak, G. (1988), *Journal of Composite Materials*, **22**, 900-916.

Roy, S., Albrecht, P. and Weidenmann, K.A. (2023), "Influence of ceramic freeze-casting temperature on the anisotropic thermal expansion behavior of corresponding interpenetrating metal/ceramic composites", *J. Mater. Eng. Perform.*, **32**(19), 8795-8806. https://doi.org/10.1007/s11665-022-07769-2.

Roy, S., Frohnheiser, J. and Wanner, A. (2020), "Effect of ceramic preform freeze-casting temperature and melt infiltration technique on the mechanical properties of a lamellar metal/ceramic composite", *J. Compos. Mater.*, **54**(15), 2001-2011. https://doi.org/10.1177/0021998319890661.

Santos, L.N.R.M., Silva, J.R.S., Cartaxo, J.M., Rodrigues, A.M., Neves, G.A. and Menezes, R.R. (2021), "Freeze-casting applied to ceramic materials: a short review of the influence of processing parameters", *Cerâmica*, **67**(381), 1-13. https://doi.org/10.1590/0366-69132021673812923.

Schukraft, J., Lohr, C. and Wiedemann, K.A. (2021), "2D and 3D in-situ mechanical testing of an interpenetrating metal ceramic composite consisting of a slurry-based ceramic foam and AlSi10Mg", *Compos. Struct.*, **263**(1), 113742, https://doi.org/10.1016/j.compstruct.2021.113742.

CC